U-Nets and Multispectral images for detecting the surface water of rivers via SAR images

Diana Orlandi[1[0009-0001-9107-4966]], Federico A. Galatolo[1[0000-0001-7193-3754]], Alessandro La Rosa[2[0000-0003-1858-1109]], Mario G. C. A. Cimino[1[0000−0002−1031−1959]], Pierfrancesco Foglia[1[0000-0001-6432-4504]], Carolina Pagli[2[0000-0002-9072-3004]], Cosimo A. Prete[1[0000-0002-8467-8198]]

[1] Dept. of Information Engineering, University of Pisa, Via G. Caruso 16, 56122, Pisa, Italy
[2] Dept. of Earth Science, University of Pisa, Via Santa Maria 53, 56126, Pisa, Italy

diana.orlandi@phd.unipi.it, alessandro.larosa@dst.unipi.it,
{federico.galatolo, mario.cimino, pierfrancesco.foglia,
carolina.pagli, antonio.prete}@unipi.it

Abstract. Global water resources are under increasing pressure due to demands from population growth and climate change. As a result, the regime of the rivers is changing and their ecosystems are threatened. Therefore, for effective water management and mitigation of hazards, it is crucial to frequently and accurately map the surface area of river water. Synthetic Aperture Radar (SAR) backscatter images at high temporal resolution are nowadays available. However, mapping the surface water of narrow water bodies, such as rivers, remains challenging due to the SAR spatial resolution (few tens of meters). Conversely, Multi-Spectral Instrument (MSI) images have a higher spatial resolution (few meters) but are affected by cloud coverage. In this paper, we present a new method for automatic detection and mapping of the surface water of rivers. The method is based on the convolutional neural network known as U-Net. To develop the proposed approach, two datasets are needed: (i) a set of Sentinel-2 MSI images, used to achieve target values; (ii) a set of Sentinel-1A SAR backscatter images, used as input values. The proposed method has been experimented to map the surface water of the Mijares river (Spain) from April 2019 to September 2022. Experimental results show that the proposed approach computes the total surface area covered by the river water with a mean absolute error equal to 0.072, which is very promising for the target application. To encourage scientific collaborations, the source code used for this work has been made publicly available.

Keywords: Surface water of rivers, Synthetic Aperture Radar, Multispectral images, Convolutional Neural Network, U-Net.

1 Introduction

In the current era of global warming and climate change, a detailed and constant monitoring of the surface water of rivers is key not only for the correct estimation and

management of river regimes but also for the mitigation of flooding risks. In the literature, free and open access Synthetic Aperture Radar (SAR) backscatter images, acquired at frequent revisit times, have been successfully applied to monitor changes of spatially large and broad surface water bodies, such as wetland and flooded areas [1, 2, 3, 4, 5]. However, mapping the surface extent of river water and its changes in time remains challenging [6] as some rivers are relatively narrow compared to the spatial resolution of SAR images (few tens of meters). In contrast, Multi-Spectral Instrument (MSI) data can offer spatial resolution on the order of a few meters, allowing for a more detailed mapping of the surface area of river water globally. However, MSI data are often affected by atmospheric noise and cloud coverage, which prevents regular observations. On the other hand, SAR satellites are capable of penetrating the atmosphere and measuring the radar backscattered from the surface of the Earth during day, night and all-weather conditions [7].

Modern deep learning techniques provide nowadays impressive results for detailed mapping and identification of features in images [8]. Recently, deep learning has shown great potential when applied to SAR data for the classification of sea and ice water, as well as for the surface water of rivers [9, 10]. In particular, the U-Net convolutional network is capable of resolving the extent of surface water bodies [11,12], by combining a semantic segmentation upon partitioning of the input image into several regions corresponding to different classes (surface water, vegetation, buildings, and so on). More recently, a U-Net was experimented to detect the surface water of a narrow river [13]. For image segmentation, depending on the type of target to recognize, the U-Net architecture provides a spatial attention mechanism that allows highlighting only the relevant parts of the image during the initial training phase, thus limiting the computational resources, resulting in a better generalization capability [13].

In this research work, an experimental study is presented and discussed, in which a U-Net architecture has been trained to return the surface water of the Mijares river in Eastern Spain. The target dataset is made via MSI images, to generate the target surface water of the river, whereas the input dataset is made via SAR backscatter images. Additional images of both datasets have been used for testing. Overall, the experiment shows that a U-Net architecture achieves adequate accuracy for the target application.

2 Study Area

Mijares is a river that flows for about 156 km in a SE direction, south of the city of Castellón de la Plana, in Eastern Spain (Fig. 1). The river is fed by two major water springs, Mas Royo and Babor in the Sierra de Gudar. Despite the permanent nature of the river, its annual regime is irregular with lows in water flow in summers and floods in autumn [14]. For this study, we focused on the last 20 km of the river (Figure 1) where Mijares flows across its alluvial plain [15]. This area is characterized by meandering sequences of fine to coarse sediments, which grade to deltaic sequences in the Almazora and Buriana plains. The alluvial deposits host the three main groundwater

reservoirs of Arenoso (93 Mm^3), Sichar (49 Mm^3) and Maria Cristina (18.4 hm^3) [15, 16].

Since the 1960s, this part of the river and its associated reservoirs have been exploited for the agricultural, industrial, and urban activities of the region, as well as for the main water supply of the Sichar dam (0.2 Mm^3) [14]. However, as a result of the changing climate [15, 17], the region is recently experiencing warmer seasons, with the total rainfall between 1980 and 2012 having decreased by 3-7% compared to the previous period, 1940-2012 [16]. Currently, the water resources in the areas are 335.7 hm^3/year and must face a water demand of 268.23 hm^3/year [18]. Furthermore, during the latest years a series of historical records in flooding events have been reached, with such events being forecasted to occur more frequently in the future [19].

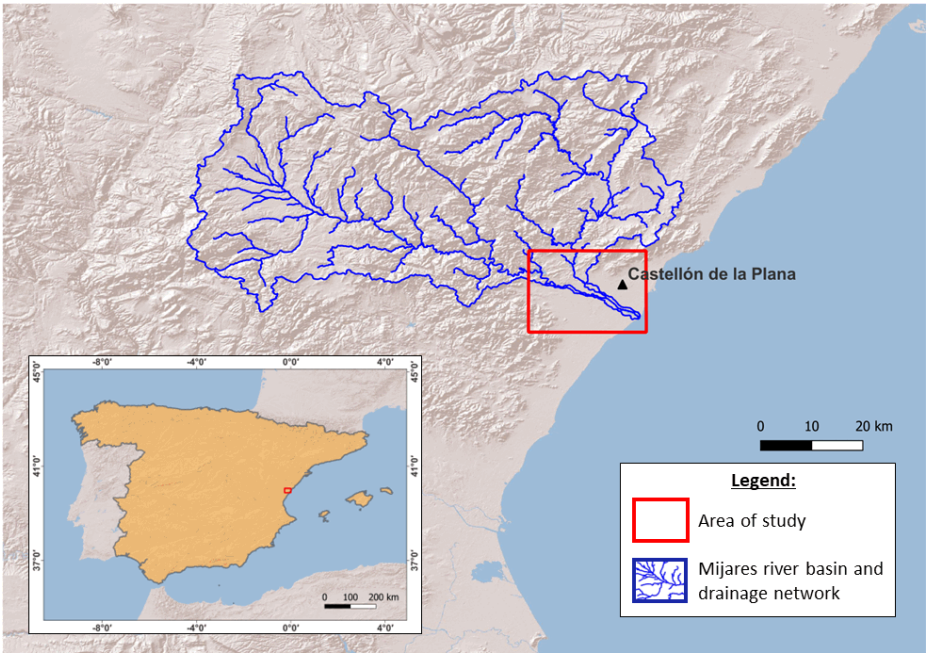

Fig. 1. Study area (red rectangle) and river drainage network [13].

3 Material and Methods

3.1 Dataset

Two independent datasets are used, consisting of MSI and SAR backscatter images acquired by the ESA satellites Sentinel-2 and Sentinel-1A, respectively. The MSI images, acquired at 10 m spatial resolution, are used to derive maps of the surface water of the Mijares river during 2019-2022. Such maps are used as target output values for

the convolutional neural network. The SAR backscattered images are used as corresponding input values.

The MSI dataset of the Mijares river consists of 36 Level 1C Sentinel-2 Multispectral images spanning the time-period between October 2019 and August 2022. In particular, the Level 1C images contain the spectral reflectance of 13 bands (B1-B12) acquired in the visible, near infrared (NIR) and short-wave infrared (SWIR) bands. The spatial resolution of the Sentinel-2 images varies between 10 m to 60 m, depending on the spectral band. In this study, bands B3 (green) and B8 (NIR) are used at a spatial resolution of 10 m. The 36 images selected have the lowest cloud coverage.

The SAR dataset consists of 36 Single Look Complex (SLC) images of the Mijares river, covering the time period between October 2019 and August 2022, and acquired from the descending orbit 008, in Interferometric Wide (IW) swath beam mode. The Sentinel-1A SAR satellite has a revisit time of 12 days and it operates in C-band, corresponding to a signal wavelength (λ) of 5.6 cm and a ground spatial resolution of 5 m $\times$ 20 m [20]. The SAR signal contains two fundamental components of the polarized radar backscattered from the Earth surface: the amplitude and the phase. While the latter provides information about the targets positions on the ground, the amplitude can be used to investigate other targets properties, such as geometry, roughness, and wetness [21]. This makes the amplitude suitable for the detection of water bodies and flooded areas [11]. As a consequence, in this study, SAR amplitude images are used. In addition, in order to minimize the effect of thermal noise and maximize the signal backscatter from narrow surfaces of river water, the VV (Vertical Emitted-Vertical Received) polarization is selected, which is commonly characterized by stronger backscatter values than the VH (Vertical Emitted-Horizontal Received) polarization [22]. A summary of the characteristics of the two datasets is reported in Table 1.

3.2 Methods

In the following chapter, we describe the proposed method for detecting the surface water of ricers, using the BPMN (Business Process Model and Notation) language, a standard graphical representation for workflows [23]. Fig.1 shows the workflows for using the water surface detector in a periodical river assessment (a) and for developing the detector itself (b).

Specifically, in Fig.1a the *detection of the water surface of the river* starts on the left, every detection period, by collecting periodical data on the river. After a number of historical data, during the assessment period a *report is generated*. The report is *checked and annotated by an expert*, and *sent to a Decision Support System* (DSS).

The core technology of the workflow in Fig. 2a is the water surface detector, which is developed for a given river according to the workflow of Fig.2b. Specifically, the development workflow starts when there is a *new river to monitor* (on top left in figure).

As a consequence, two parallel activities are carried out, i.e., *get MSI image and get SAR image*, respectively. Each type of image is followed by a different sequence of tasks. The next two subsections illustrate the two kinds of data ingestion and preparation.

Table 1. Sentinel datasets.

Satellite	Sentinel-2	Sentinel-1A
Product Level	Multispectral Instrument (MSI) – Level-1C	Single Look Complex (SLC)
Tiles	T31TBE, T30TYK	-
Spatial Resolution (m)	10 × 10	5 × 20
Orbit	-	Descending (path 8, frame 458)
Acquisition mode	-	Interferometric Wide swath (IW)
Revisit time	-	12 days
Polarization	-	VV

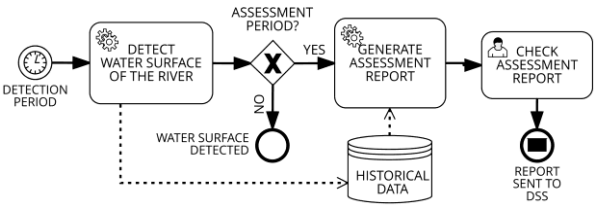

(a)

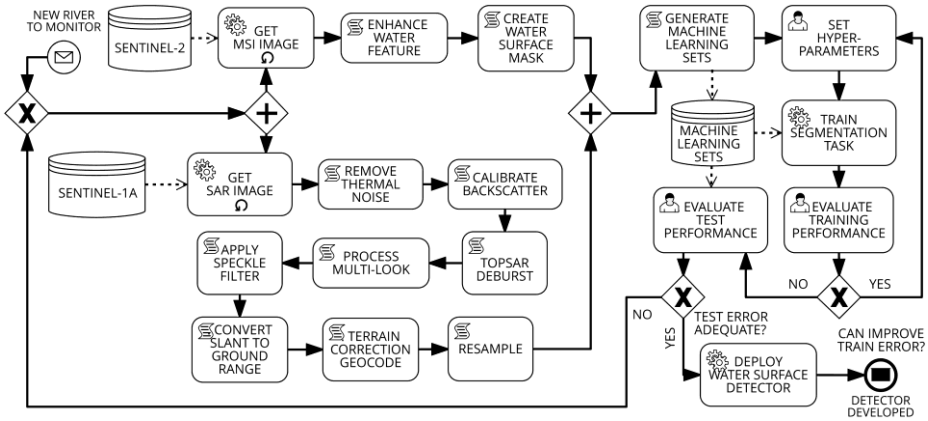

(b)

Fig. 2. The BPMN workflows for detecting the surface water of rivers: (a) the workflow for developing the detector; (b) the workflow for using the detector in a periodical river assessment.

MSI image ingestion and preparation

A number of MSI images are first collected from the Sentinel-2 web service. Subsequently, to *enhance the water feature*, the Normalized Difference Water Index (NDWI) is calculated, using the spectral reflectance of B3 and B8 bands, as follows [24]:

$$NDWI = \frac{(B3-B8)}{(B3+B8)} \quad (1)$$

In the formula, the combination of visible green (B3) and near-infrared (B8) bands highlights the water content of different water bodies [24]. In the resulting NDWI maps, a pixel value can vary between -1 and +1, with lower values corresponding to non-aqueous surfaces (soil or vegetation) and higher values corresponding to water. Finally, to *create the water surface mask* of the river, the pixels with NDWI values larger than a threshold are selected. In the case of the Mijares river, 36 MSI images are selected, and the threshold is set to -0.1. This threshold is found by comparing each of the 36 NDWI maps to its corresponding optical image, where the surface water of the Mijares river can be seen directly. As a result, 36 masks with two classes of surfaces, "water" and "non-water" are provided, 28 for training and 8 for testing.

In addition, to reduce the computational cost of the U-Net training, a single Water Surface Mask (WSM) of the river is created for the entire study period, by selecting pixels classified as "water" in at least one NDWI image. The WSM is helpful to keep only the water pixels related to the river, instead of considering the whole study area.

SAR backscatter image ingestion and preparation

The SAR SLCs backscatter images are first collected from the Sentinel-1A web service. Subsequently, a series of pre-processing steps are carried out via the Sentinel Application Platform [25]. Specifically, a number of corresponding SAR amplitude images are acquired in the same time window selected for the MSI images. Then, for each SAR amplitude image, *a thermal noise filter* on the VV amplitude images is carried out, normalizing the backscatter signal. Subsequently, the *calibrated backscattered coefficient* ($\sigma 0$) is calculated: it represents the normalized radar backscatter from a distributed target [26, 27]. Discontinuities between sub-swaths are then removed by merging the bursts through the *TOPSAR-Deburst* preprocessing. A *multi-looking filter* followed by a *speckle noise filter* are then applied: specifically, three different types of filters have been tested: Lee, IDAN and Lee Sigma [28]. In the case in point, the Lee Sigma filter has provided the best result, while IDAN and Lee have showed higher residual noise, as represented in Fig. 3. Subsequently, the filtered images are projected from *Slant Range geometry to Ground Range* (SRGR), and then *geocoded* using a 1 arc-sec (30 m) Shuttle Radar Topography Mission (SRTM) Digital Elevation Model (DEM) [29]. Finally, to achieve a pixel-by-pixel image matching, the SAR images are *resampled* to 10 m pixel size as the MSI images.

SAR amplitude semantic segmentation via U-Net

After the MSI and SAR images ingestion and preparation, the *machine learning sets are generated*, made of 36 prepared SAR images, with 36 corresponding water segmentation images. As a consequence, the image segmentation task consists in separating a given SAR image pixels into "water" and "non-water" classes. The task is developed via a fully Convolutional Neural Network, known as U-Net [8].

In the literature, the U-Net architecture is well-known for biomedical image segmentation, but widespread applications in various research fields have been successfully developed: forest mapping [30], earthquakes damage mapping [31], coastal wetland classification [32], and so on. A U-Net exhibits a low computational demand, an accurate segmentation compared to other approaches, and a superior capability of working with a small training dataset [8].

An important step related to the U-Net development is the *setting of hyperparameters*. A detailed description of the final U-Net hyperparameters settings achieved for the Mijares river is presented in Table 2. It is worth noting that the hyperparameters setting is an iterative task, carried out after an improvement/optimization process, strongly depending on the complexity of the machine learning set.

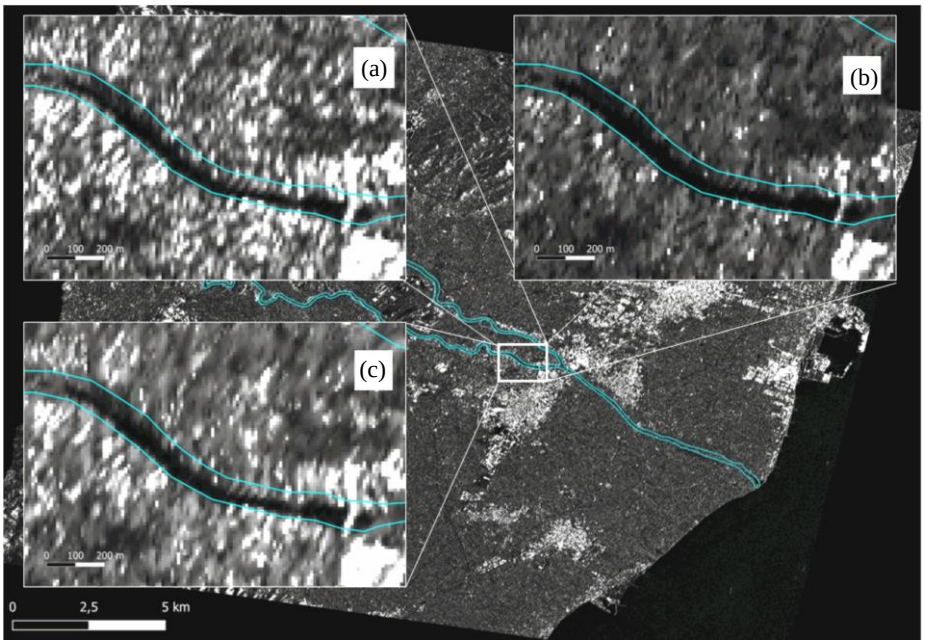

Fig. 3. SAR backscatter image of the Mijares river (background image) and detail of the SAR backscatter image after speckle filtering [13]. (a) SAR backscatter image after Lee filter; (b) SAR backscatter image after IDAN filter; (c) SAR backscatter image after Lee Sigma.

In the subsequent *training of the segmentation task*, the U-Net optimizes its internal parameters to improve the mapping between the input samples (i.e., the 28 prepared SAR backscatter images) and the corresponding target output samples (i.e., the 28 water/non-water surface maps generated from MSI images).

Specifically, the U-Net calculates the probability that a pixel belongs to a class. For this purpose, the U-Net adopts an encoding path that detects the features from the input dataset, and a decoding path that generates the output segmentation map. Both the encoding and decoding paths consist of a series of layers that are repeatedly applied on randomly sampled kernels of both the input dataset and the training dataset. In particular, the encoding path consists of a convolutional layer and a max pooling layer, which reduces the spatial dimension of the input maps multiple times, allowing the network to capture increasingly complex features. For the convolution operation, 128 × 128 pixels kernels are used. The decoding path initially applies an up-convolutional layer, which increases the spatial dimensions of the feature maps. Subsequently, it concatenates the output with the corresponding feature map obtained from the encoding path. This allows the network to compare the low-level and high-level features. This process of up-convolution and concatenation is repeated multiple times, allowing the network to refine the segmentation map.

Table 2. U-Net hyperparameters settings [13].

Parameter	Description	Value(s)
dim	no. initial channels	8
dim mults	no. channels multipliers	[1, 2, 4]
blocks per stage	no. convolutional operations per stage	[2, 2, 2]
self-attentions per stage	no. self-attention blocks per stage	[0, 0, 1]
channels	input channels	1
resnet groups	no. normalization groups	2
consolidate upsample fmaps	feature maps consolidation	true
weight standardize	weight standardization	false
attention heads	no. attention heads	2
attention dim head	size of attention head	16
training window size	window size of training samples	128
training batch size	no. of samples per iteration	32
learning rate	amount of weight change in response to the error	0.001

The final output is a segmented image that assigns a class to each pixel in the input image. In the case in point, the segmented image is a map of the surface water of the Mijares river, where pixels pertaining to surface water of the river have a value of 1, while the other pixels are 0.

For the segmentation task of the Mijares river, the training phase is made by a subset of 28 of the 36 total images, while the remaining 8 images are used for testing. The performance of the predictions has been sampled between 5K and 50K iterations, on 10 test images acquired at different epochs, using an iteration stepping of 5K runs. Fig.

4 illustrates some significant examples of mapping of the surface water of the Mijares river. In particular, Fig. 4a and Fig. 4b show the SAR image on Jan 20, 2020 and the corresponding MSI optical image (i.e., with lowest cloud coverage), on Feb 10, 2020, respectively. It is worth remembering that optical images are often affected by atmospheric noise and cloud coverage, which prevents regular observations. Fig. 4c and Fig. 4d show the MSI-derived target output of the surface water (black), on Feb 10, 2020, and the Water Surface Mask generated for the entire study period via the training set, respectively. Finally, Fig. 3e and Fig.3f illustrate the outputs of the U-Net on Jan 20, 2020, after 5K and 20K iterations, respectively: as the number of the iterations increases, the map of the surface water includes more details.

After *training the segmentation task*, in Figure 2b the workflow continues with the performance evaluation: if the error can be improved, the hyperparameters setting is repeated, and so on. Otherwise, the U-Nete is evaluated on the test set: if the test error is adequate, the water surface detector is finally deployed and ready for use in the periodical river assessment. Otherwise, the workflow restarts from the beginning, by collecting a new data set.

4 Performance evaluation and discussion

To carry out the experimentation of the proposed research, an open-source implementation of the U-Net has been exploited [33] to develop the workflow of Fig. 2b. To encourage scientific collaborations, the source code used for this work has been made publicly available [34].

In Fig. 5 the graph of the cross-entropy loss vs. number of iterations is represented, for the first 30K iterations. The figure highlights that the training performance is effective after 5K iterations.

In order to measure the effectiveness of the approach, the total surface area covered by river water has been calculated, hereafter referred to as Normalized River Water Extent (NRWE), for both SAR and MSI timeseries. Fig. 6 shows an excerpt of the two timeseries, with a clear similar progress. Overall, the Mean Absolute Error (MAE) between the SAR and MSI based NRWE is equal to 0.072, which is very effective for the target application.

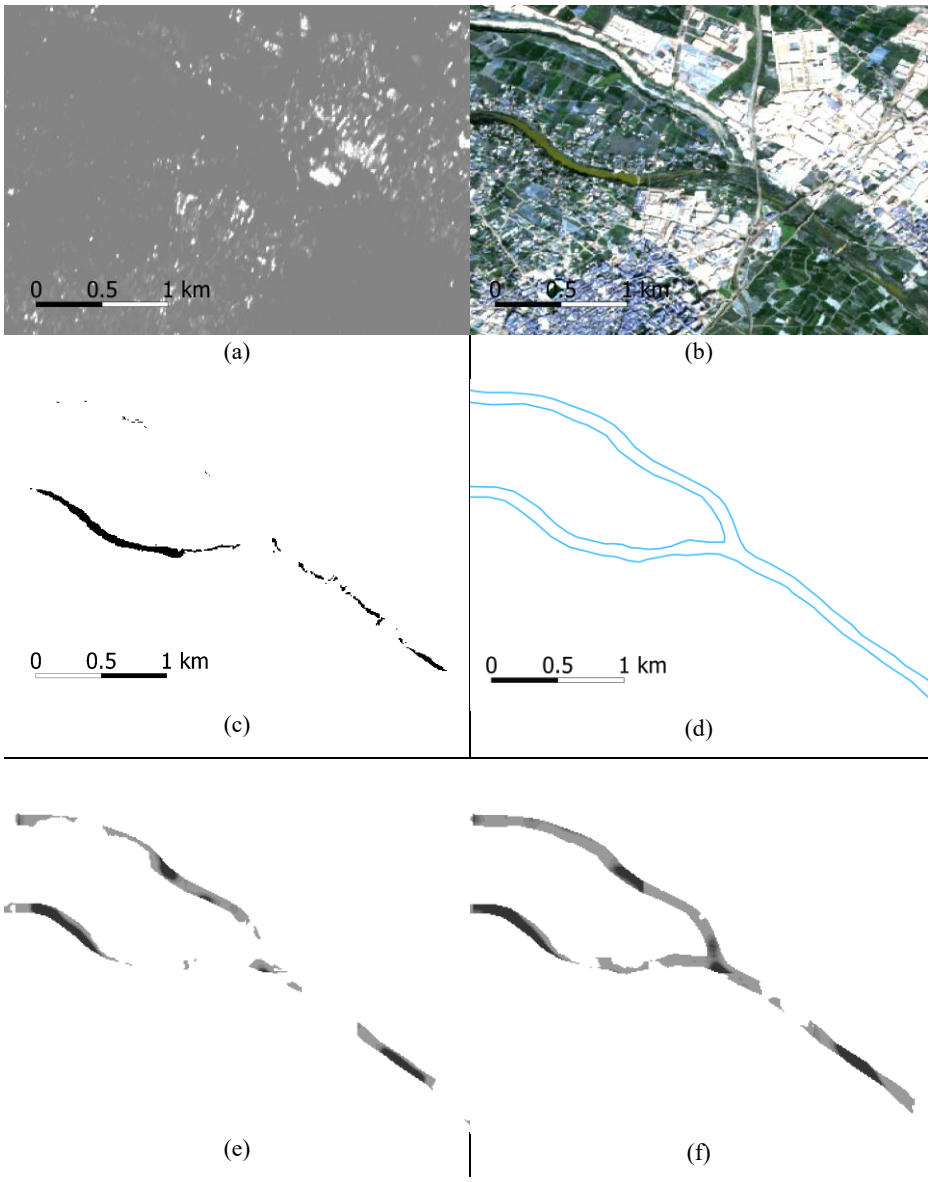

Fig. 4. Example of mapping of the surface water of the Mijares river: (a) Sentinel-1 SAR backscatter input image acquired on Jan 20, 2020; (b) Sentinel-2 MSI optical image acquired on Feb 10, 2020; (c) target output of the surface water (black) derived from NDWI map, calculated via the MSI image acquired on Feb 10, 2020; (d) Water Surface Mask generated via the training set; (e) output of the U-Net on Jan 20,2020 after 5K iterations; (f) output of the U-Net on Jan 20, 2020 after 20K iterations.

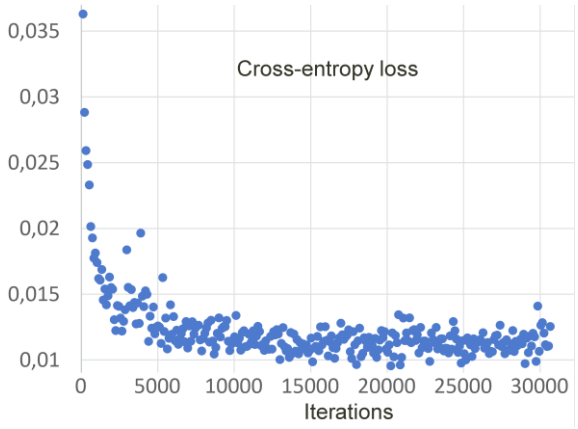

Fig. 5. Cross-entropy loss vs number of iterations [13]

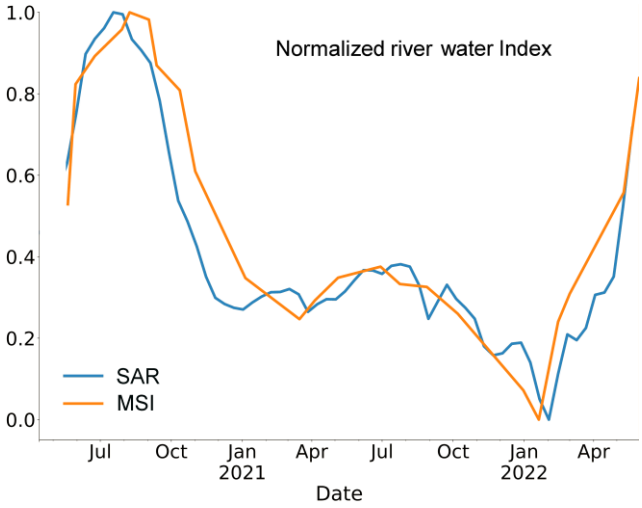

Fig. 6. Normalized River Water Index [13].

5 Conclusions

In this research work, the U-Net Convolutional Neural Network has been proposed to detect the surface water of rivers via satellite data, using MSI and SAR images as target and input data, respectively.

The paper illustrates the proposed method using the Mijares river in Spain as a pilot study area. For the sake of reproducibility, a workflow has been formalized and illustrated in BPMN language, to detail the Sentinel datasets and their preprocessing, the development of the U-Net for the segmentation task, the hyperparameters settings, as well as the periodical river monitoring for feeding a decision support system.

The experimental studies on the Mijares river are promising, with a mean absolute error of the total water surface area equal to 0.072, although the presented approach represents an initial step towards a more comprehensive experimentation.

Further investigations can involve the extension of the time period of analysis, with the aim of monitoring the temporal fluctuations and climate change impacts on river ecosystems. To encourage scientific collaborations, the source code used for this work has been made publicly available [34].

Acknowledgements

This work has been partially supported by: (i) the National Center for Sustainable Mobility MOST/Spoke10, funded by the Italian Ministry of University and Research, in the framework of the National Recovery and Resilience Plan; (ii) the PRA_2022_101 project “Decision Support Systems for territorial networks for managing ecosystem services”, funded by the University of Pisa; (iii) the Ministry of University and Research (MUR) as part of the PON 2014-2020 “Research and Innovation" resources – Green/Innovation Action – DM MUR 1061/2022"; (iv) the Italian Ministry of University and Research (MUR), in the framework of the "Reasoning" project, PRIN 2020 LS Programme, Project number 2493 04-11-2021; (v) the Italian Ministry of Education and Research (MIUR) in the framework of the FoReLab project (Departments of Excellence).

References

1. Botha, E.J., Anstee, J.M., Sagar, S., Lehmann, E., Medeiros, T.A.G.: Classification of Australian waterbodies across a wide range of optical water types. Remote Sens. 12 (2020). https://doi.org/10.3390/RS12183018.
2. Frappart, F., Zeiger, P., Betbeder, J., Gond, V., Bellot, R., Baghdadi, N., Blarel, F., Darrozes, J., Bourrel, L., Seyler, F.: Automatic detection of inland water bodies along altimetry tracks for estimating surface water storage variations in the congo basin. Remote Sens. 13, 1–22 (2021). https://doi.org/10.3390/rs13193804.
3. Carreño-Conde, F., De Mata Muñoz, M.: Flood monitoring based on the study of Sentinel-1 SAR images: The Ebro River case study. Water (Switzerland). 11, 1–25 (2019). https://doi.org/10.3390/w11122454.
4. Quirós, E., Gagnon, A.S.: Validation of flood risk maps using open source optical and radar satellite imagery. Trans. GIS. 24, 1208–1226 (2020). https://doi.org/10.1111/tgis.12637.

5. Tran, K.H., Menenti, M., Jia, L.: Surface Water Mapping and Flood Monitoring in the Mekong Delta Using Sentinel-1 SAR Time Series and Otsu Threshold. Remote Sens. 14, (2022). https://doi.org/10.3390/rs14225721.
6. Filippucci, P., Brocca, L., Bonafoni, S., Saltalippi, C., Wagner, W., Tarpanelli, A.: Sentinel-2 high-resolution data for river discharge monitoring. Remote Sens. Environ. 281, 113255 (2022). https://doi.org/10.1016/j.rse.2022.113255.
7. Kumar, D. Urban objects detection from C-band synthetic aperture radar (SAR) satellite images through simulating filter properties. Sci Rep 11, 6241 (2021). https://doi.org/10.1038/s41598-021-85121-9
8. Ronneberger, O., Fisher, P., Brox, T.: Convolutional Networks for Biomedical Image Segmentation. In: International Conference on Medical image computing and computer-assisted intervention (2015). https://doi.org/https://doi.org/10.48550/arXiv.1505.04597.
9. Jiang, M., Xu, L., Clausi, D.A.: Sea Ice–Water Classification of RADARSAT-2 Imagery Based on Residual Neural Networks (ResNet) with Regional Pooling. Remote Sens. 14, (2022). https://doi.org/10.3390/rs14133025.
10. Orlandi, D., Galatolo, F.A., Cimino, M.G.C.A., Rosa, A. La, Pagli, C., Perilli, N.: Enhancing land subsidence awareness via InSAR data and Deep Transformers. Proc. - 2022 IEEE Int. Conf. Cogn. Comput. Asp. Situat. Manag. CogSIMA 2022. 98–103 (2022). https://doi.org/10.1109/CogSIMA54611.2022.9830661.
11. Wang, G., Wu, M., Wei, X., Song, H.: Water identification from high-resolution remote sensing images based on multidimensional densely connected convolutional neural networks. Remote Sens. 12, (2020). https://doi.org/10.3390/rs12050795.
12. Wang, J., Wang, S., Wang, F., Zhou, Y., Wang, Z., Ji, J., Xiong, Y., Zhao, Q.: FWENet: a deep convolutional neural network for flood water body extraction based on SAR images. Int. J. Digit. Earth. 15, 345–361 (2022). https://doi.org/10.1080/17538947.2021.1995513.
13. Orlandi, D.; Galatolo, F.; Cimino, M.; Pagli, C.; Perilli, N.; Pompeu, J. and Ruiz, I. (2023). Using Deep Learning and Radar Backscatter for Mapping River Water Surface. In Proceedings of the 9th International Conference on Geographical Information Systems Theory, Applications and Management - GISTAM; ISBN 978-989-758-649-1; ISSN 2184-500X, SciTePress, pages 216-221. DOI: 10.5220/0011975000003473
14. Macian-Sorribes H., Pulido-Velazquez M., and Tilmant A. (2015) Definition of efficient scarcity-based water pricing policies through stochastic programming. Hydrol. Earth Syst. Sci., 19, 3925–3935, 2015 www.hydrol-earth-syst-sci.net/19/3925/2015 doi:10.5194/hess-19-3925-2015
15. Garófano-Gómez, V., Martínez-Capel, F., Bertoldi, W., Gurnell, A., Estornell, J., Segura-Beltrán, F.: Six decades of changes in the riparian corridor of a mediterranean river: A synthetic analysis based on historical data sources. Ecohydrology. 6, 536–553 (2013). https://doi.org/10.1002/eco.1330.
16. MedECC: Spatial characterization of the seawater upconing process in a coastal Mediterranean aquifer (Plana de Castellón, Spain): evolution and controls. In: Cramer, W., Guiot, J., and Marini, K. (eds.) Union for the Mediterranean, Plan Bleu, UNEP/MAP, Marseille, France. p. 632 (2020). https://doi.org/10.1007/s12665-016-5531-7.
17. MedECC: Climate and Environmental Change in the Mediterranean Basin – Current Situation and Risks for the Future. First Mediterranean Assessment Report. (2020). https://doi.org/10.5281/zenodo.4768833.
18. Confederación Hidrográfica del Júcar: Plan Hidrológico de la Demarcación Hidrográfica del Júcar. Revisión de tercer ciclo (2021-2027). (2019).
19. Masson-Delmotte, V., Zhai, P., Chen, Y., Goldfarb, L., Gomis, M.I., Matthews, J.B.R., Berger, S., Huang, M., Yelekçi, O., Yu, R., Zhou, B., Lonnoy, E., Maycock, T.K.,

Waterfield, T., Leitzell, K., Caud, N.: Summary for Policymakers. In Climate Change 2021: The Physical Science Basis. Contribution of Working Group I to the Sixth Assessment Report of the Intergovernmental Panel on Climate Change. (2021).
20. Yague-Martinez, N., Prats-Iraola, P., Gonzalez, F.R., Brcic, R., Shau, R., Geudtner, D., Eineder, M., Bamler, R.: Interferometric Processing of Sentinel-1 TOPS Data. IEEE Trans. Geosci. Remote Sens. 54, 2220–2234 (2016). https://doi.org/10.1109/TGRS.2015.2497902.
21. Geudtner, D., Torres, R., Snoeij, P., Ostergaard, A., Navas-Traver, I.: Sentinel-1 mission capabilities and SAR system calibration. IEEE Natl. Radar Conf. - Proc. 0–3 (2013). https://doi.org/10.1109/RADAR.2013.6586141.
22. Dzurisin, D., Lu, Z.: Interferometric synthetic-aperture radar (InSAR). In: Volcano Deformation. Geodetic Monitoring Techniques. pp. 153–194. Springer-Verlag Berlin Heidelberg New York (2007).
23. Ciaramella, A., Cimino, M. G., Lazzerini, B., Marcelloni, F. (2009). Using BPMN and tracing for rapid business process prototyping environments. In International Conference on Enterprise Information Systems (Vol. 1, pp. 206-212). SCITEPRESS.
24. McFeeters, S.K.: The use of the Normalized Difference Water Index (NDWI) in the delineation of open water features. Int. J. Remote Sens. 25, 687–711 (1996). https://doi.org/10.1080/01431169608948714.
25. SNAP - ESA Sentinel Application Platform v2.0.2, http://step.esa.int
26. Tamkuan, N., Nagai, M.: Alos-2 and sentinel-1 backscattering coefficients for water and flood detection in nakhon phanom province, northeastern thailand. Int. J. Geoinformatics. 17, 39–48 (2021). https://doi.org/10.52939/ijg.v17i3.1895.
27. Laur, H., Bally, P., Meadows, P., Sanchez, J., Schaettler, B., Lopinto, E., Esteban, D.: Derivation of the backscattering coefficient in ESA ERS SAR PRI Products. In: ESA Document No: ES-TN-RS-PM-HL09 05. p. 53 (2004).
28. Tran, K.H.; Menenti, M.; Jia, L. Surface Water Mapping and Flood Monitoring in the Mekong Delta Using Sentinel-1 SAR Time Series and Otsu Threshold. Remote Sens. 2022, 14, 5721. https://doi.org/10.3390/rs14225721
29. Farr, T.G., Rosen, P., Caro, E., Crippen, R., Duren, R., Hensley, S., Kobrick, M., Paller, M., Rodriguez, E., Roth, L., Seal, D., Shaffer, S., Shimada, J., Umland, J., Werner, M., Oskin, M., Burbank, D., Alsdorf, D.: The Shuttle Radar Topoghraphy Mission. Rev. Geophys. 45 (2007). https://doi.org/10.1029/2005RG000183.
30. Wagner, F.H., Sanchez, A., Tarabalka, Y., Lotte, R.G., Ferreira, M.P., Aidar, M.P.M., Gloor, E., Phillips, O.L., Aragão, L.E.O.C.: Using the U-net convolutional network to map forest types and disturbance in the Atlantic rainforest with very high resolution images. Remote Sens. Ecol. Conserv. 5, 360–375 (2019). https://doi.org/10.1002/rse2.111.
31. Bai, Y., Mas, E., Koshimura, S.: Towards operational satellite-based damage-mapping using U-net convolutional network: A case study of 2011 Tohoku Earthquake-Tsunami. Remote Sens. 10 (2018). https://doi.org/10.3390/rs10101626.
32. Dang, K.B., Nguyen, M.H., Nguyen, D.A., Phan, T.T.H., Giang, T.L., Pham, H.H., Nguyen, T.N., Van Tran, T.T., Bui, D.T.: Coastal wetland classification with deep u-net convolutional networks and sentinel-2 imagery: A case study at the tien yen estuary of vietnam. Remote Sens. 12, 1–26 (2020). https://doi.org/10.3390/rs12193270.
33. Wang, P.: Implementation of a Unet complete with efficient attention as well as the latest research findings, https://github.com/lucidrains/x-unet, (2023).
34. Galatolo, F.A.: Gistam2023, github.com/galatolofederico/gistam2023, (2023).